Journal of Volcanology and Geothermal Research 302 (2015) 102–116

Contents lists available at ScienceDirect

Journal of Volcanology and Geothermal Research

journal homepage: www.elsevier.com/locate/jvolgeores

Variability in composition and physical properties of the sedimentary basement of Mt Etna, Italy

Sebastian Wiesmaier [a,b,*], Michael J. Heap [c], Stefano Branca [d], H. Albert Gilg [e], Ulrich Kueppers [a], Kai-Uwe Hess [a], Yan Lavallée [f], Donald B. Dingwell [a]

[a] Department of Earth and Environmental Sciences, Ludwig-Maximilians-Universität (LMU) München, Theresienstr. 41/III, 80333 Munich, Germany
[b] GEOVOL, Universidad de Las Palmas de Gran Canaria, 35017 Las Palmas de Gran Canaria, Spain
[c] Équipe de Géophysique Expérimentale, Institut de Physique de Globe de Strasbourg (UMR 7516 CNRS, Université de Strasbourg/EOST), 5 rue René Descartes, 67084 Strasbourg cedex, France
[d] Istituto Nazionale di Geofisica e Vulcanologia, Osservatorio Etneo, Piazza Roma 2, 95125 Catania, Italy
[e] Lehrstuhl für Ingenieurgeologie, Technische Universität München, Arcisstr. 21, 80333 Munich, Germany
[f] Earth, Ocean and Ecological Sciences, University of Liverpool, Liverpool L69 3GP, United Kingdom

ARTICLE INFO

Article history:
Received 4 March 2015
Accepted 15 June 2015
Available online 19 June 2015

Keywords:
Uniaxial compressive strength
Young's modulus
Microstructure
Porosity
P-wave velocity
Mineralogical composition

ABSTRACT

The sub-volcanic basement at Mt Etna (Italy) comprises thick sedimentary sequences. An understanding of the physical, mechanical, and microstructural properties of these sequences, and an appreciation of their variability, is important for an accurate assessment of the structural stability of Mt Etna. Here, we present a combined field and laboratory study in which we explore the extent of variability of the materials comprising the sedimentary basement of Mt Etna. To this end, we sampled twelve different lithological units that span the sediments of the Apenninic-Maghrebian Chain (from both the Sicilide and Ionides sequences) and the Hyblean Plateau. X-ray diffraction analysis of the blocks collected show that calcite and quartz are the predominant mineral phases. Textural analysis highlights the wide variability in rock microstructures, with features such as the presence/absence of fractures or veins, pore size and shape, and grain size and shape varying tremendously between the samples. One consequence of this microstructural, textural, and mineralogical variability is that the rock units are characterised by very different values of porosity, P-wave velocity, uniaxial compressive strength, and static Young's modulus. For example, strength and Young's modulus vary by a factor of twenty and an order of magnitude, respectively. Our study affirms the vast heterogeneity of the sub-volcanic sedimentary basement of Mt Etna and, on this basis, we urge caution when selecting potentially oversimplified input parameters for models of flank stability.

© 2015 Elsevier B.V. All rights reserved.

1. Introduction

The basement of Mt Etna (Italy) hosts a wide variety of sedimentary lithologies (e.g., Lentini, 1982; Grasso and Lentini, 1982; Pedley and Grasso, 1992; Lentini et al., 1996; Lentini et al., 2006; Branca et al., 2011; Branca and Ferrara, 2013). While the physical and mechanical properties of the volcanic rocks at Mt Etna have been the focus of a number of recent laboratory studies (e.g., Vinciguerra et al., 2005; Stanchits et al., 2006; Benson et al., 2007; Heap et al., 2009, 2011; Fortin et al., 2011), experimental studies on the properties of the sub-volcanic sedimentary substrata are relatively scarce (e.g., Mollo et al., 2011; Heap et al., 2013). This is despite the fact that the physical and mechanical properties of these sedimentary units, and an appreciation of their variability, is of central importance for understanding volcano spreading, deformation, and stability (e.g., Van Wyk De Vries and Borgia, 1996; Van Wyk De Vries and Francis, 1997; Tibaldi and Lagmay, 2006) and for modelling flank instability (Apuani et al., 2013 and references therein). Edifice stability is of particular importance at Mt Etna which undergoes continuous large scale sliding of the eastern flank (Borgia et al., 1992, 2000a, b; Bonforte and Puglisi, 2003, 2006; Rust et al., 2005; Palano et al., 2008, 2009; Bonforte et al., 2011; Acocella et al., 2013). Laboratory studies, so far, have provided data on rocks from two of the principal sedimentary successions under Mt Etna: a marly limestone belonging to the Apennine Maghrebian Chain (Polizzi Formation, Sicilide Unit) (Mollo et al., 2011) and a bio-calcarenite from the Hyblean Plateau (Monti Climiti Formation, Sortino Group) (Heap et al., 2013). While these studies offer useful insights, so few lithologies do not accurately capture the vast heterogeneity of the sedimentary substrata at Mt Etna. Here, we present a systematic field and laboratory study to assess the variability in mineralogical composition, texture, and physical properties of sedimentary rocks from the sub-volcanic basement of Mt Etna. We also include an estimate of the volume percentage of competent versus loose material for some of the sedimentary units.

* Corresponding author: Department of Earth and Environmental Sciences, Ludwig-Maximilians-Universität (LMU) München, Theresienstr. 41/III, 80333 Munich, Germany.
E-mail address: sebastian.wiesmaier@min.uni-muenchen.de (S. Wiesmaier).

http://dx.doi.org/10.1016/j.jvolgeores.2015.06.011
0377-0273/© 2015 Elsevier B.V. All rights reserved.

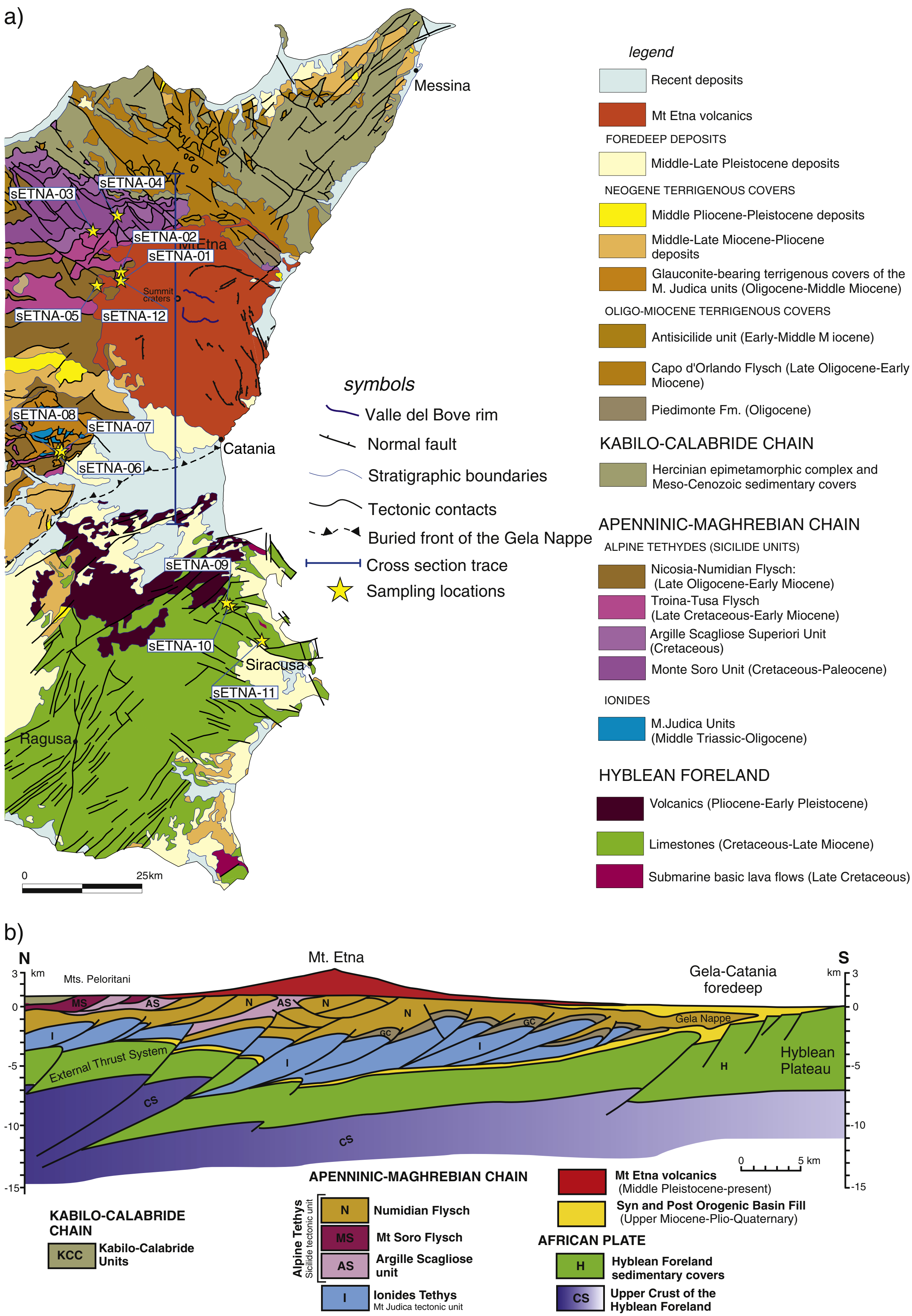

a)
Messina
sETNA-04
sETNA-03
sETNA-02
Mt Etna
sETNA-01
Summit craters
sETNA-05
sETNA-12
sETNA-08
sETNA-07
Catania
sETNA-06
sETNA-09
sETNA-10
Siracusa
sETNA-11
Ragusa
0
25km
symbols
Valle del Bove rim
Normal fault
Stratigraphic boundaries
Tectonic contacts
Buried front of the Gela Nappe
Cross section trace
Sampling locations
legend
Recent deposits
Mt Etna volcanics
FOREDEEP DEPOSITS
Middle-Late Pleistocene deposits
NEOGENE TERRIGENOUS COVERS
Middle Pliocene-Pleistocene deposits
Middle-Late Miocene-Pliocene deposits
Glauconite-bearing terrigenous covers of the M. Judica units (Oligocene-Middle Miocene)
OLIGO-MIOCENE TERRIGENOUS COVERS
Antisicilide unit (Early-Middle M iocene)
Capo d'Orlando Flysch (Late Oligocene-Early Miocene)
Piedimonte Fm. (Oligocene)
KABILO-CALABRIDE CHAIN
Hercinian epimetamorphic complex and Meso-Cenozoic sedimentary covers
APENNINIC-MAGHREBIAN CHAIN
ALPINE TETHYDES (SICILIDE UNITS)
Nicosia-Numidian Flysch: (Late Oligocene-Early Miocene)
Troina-Tusa Flysch (Late Cretaceous-Early Miocene)
Argille Scagliose Superiori Unit (Cretaceous)
Monte Soro Unit (Cretaceous-Paleocene)
IONIDES
M.Judica Units (Middle Triassic-Oligocene)
HYBLEAN FORELAND
Volcanics (Pliocene-Early Pleistocene)
Limestones (Cretaceous-Late Miocene)
Submarine basic lava flows (Late Cretaceous)
b)
N
S
km
Mts. Peloritani
Mt. Etna
Gela-Catania foredeep
MS
AS
N
GC
Gela Nappe
I
External Thrust System
CS
H
Hyblean Plateau
3
0
-5
-10
-15
0
5 km
APENNINIC-MAGHREBIAN CHAIN
Alpine Tethys
Sicilide tectonic unit
N Numidian Flysch
MS Mt Soro Flysch
AS Argille Scagliose unit
I Ionides Tethys
Mt Judica tectonic unit
KABILO-CALABRIDE CHAIN
KCC Kabilo-Calabride Units
Mt Etna volcanics (Middle Pleistocene-present)
Syn and Post Orogenic Basin Fill (Upper Miocene-Plio-Quaternary)
AFRICAN PLATE
H Hyblean Foreland sedimentary covers
CS Upper Crust of the Hyblean Foreland

Table 1
Sampled units and sampling locations. Three "greater units" relevant for the stability of Etna have been sampled: (a) Apenninic-Maghrebian (AMC) Sicilide, (b) AMC Ionides and, (c) the Hyblean foreland. The column "Unit description" provides a brief note of macroscopic features of the respective lithology.

Sample#	Greater unit	Unit	Unit description	UTM 33S East	UTM 33S North	Uncertainty
sETNA-01	Apenninic-Maghrebian Chain Sicilide	Troina-Tusa flysch	Alternation of cinder-grey marl and white marly limestone. The medium-low interval presents siltstone and grey micaceous arenite.	486948	4183484	(±14)
sETNA-02	Apenninic-Maghrebian Chain Sicilide	Nicosia-Numidian flysch	Chaotic yellowish quartzarenites and brown clays; basal levels of varicoloured clays and marls.	487213	4184737	(±12)
sETNA-03	Apenninic-Maghrebian Chain Sicilide	Argille Scagliose Superiori	Chaotic variegated and varicolored clay with calcilutites and graded calcarenites; Not sampled: siltite lenses, qz-arenite and micro-conglomerate (all volumetrically subordinate)	483110	4188843	(±5)
sETNA-04	Apenninic-Maghrebian Chain Sicilide	Monte Soro flysch	Dark marly clays and marly limestones, grading upward to greenish-yellowish quartzarenites. Thick green qz-arenitic layers embedded in clay-rich material (Black shale not sampled, too incoherent)	485454	4194573	(±46)
sETNA-05	Apenninic-Maghrebian Chain Sicilide	Numidian flysch	Chaotic yellowish quartzarenites and brown clays; basal levels of varicoloured clays and marls.	482353	4184857	(±9)
sETNA-06	Apenninic-Maghrebian Chain Ionides	Mt Judica, Scillato formation	Calcilutites, Cherty limestones and gray and whitish gray marly limestone. One of two main units of the Ionides. The other one, marly clay ("0 mm"), is loose material (sample 8)	474125	4149727	(±15)
sETNA-07	Apenninic-Maghrebian Chain Ionides	Mt Judica, Crisanti formation	Alternation of radiolarites, reddish siliceous shales and ftaniti. Ca. 100 m thickness Embedded	473726	4151108	(±12)
sETNA-08	Apenninic-Maghrebian Chain Ionides	Mt Judica, Catenanuova formation	Marly clay from brown to grey-green and glauconitic sandstone	473979	4151243	(±10)
sETNA-09	Hyblean foreland	Mt Climiti formation	Algal calcarenites and calcirudites with Clypeaster	509150	4118577	(±9)
sETNA-10	Hyblean foreland	Mt Climiti formation	Algal calcarenites and calcirudites with Clypeaster	508359	4118297	(±6)
sETNA-11	Hyblean foreland	Priolo formation	Rudistid limestones, with corals, algae, and gastropods	515820	4110234	(±13)
sETNA-12	Apenninic-Maghrebian Chain Sicilide	Troina-Tusa flysch	Alternation of cinder-grey marl and white marly limestone. The medium-low interval presents siltstone and grey micaceous arenite.	486948	4183484	(±14)
ML	Additional sample for comparison (from Mollo et al., 2011)	Polizzi formation (AMC, Sicilide)		n/a		

We first provide an overview of the geological and tectonic setting of Mt Etna and its sedimentary substrata. We then detail the results of our field and sample collection campaign and present the textural and mineralogical analysis of our experimental materials. The results of our laboratory measurements (porosity, elastic wave velocity, uniaxial compressive strength, static Young's modulus) are then presented. Finally, we outline the implications of our data for large scale deformation at Mt Etna and as input parameters for models of flank instability.

2. Geological setting

2.1. Tectonic and geological setting of eastern Sicily

The orogenic belt of eastern Sicily is composed of different structural domains formed during the collision of the Eurasian and African plates during the Neogene (Fig. 1a). The belt consists of two distinct superimposed chains forming a duplex structure exposed in northeastern Sicily (Lentini et al., 2006). The Kabilo-Calabride Chain, mostly composed of Hercynian crystalline rocks with the remnants of the original Meso-Cenozoic sedimentary cover, represents the uppermost element that tectonically overlies the so-called Apenninic-Maghrebian Chain (AMC). These two chains are overlain by the Neogene and Oligo-Miocene terrigenous covers that are represented by the Antisicilide unit, the Piedimonte Formation and by the Capo d'Orlando flysch, respectively. Geophysical data have shown that, in northeastern Sicily, the AMC allochtonous hangingwall is overthrust onto the deep-seated carbonaceous sedimentary cover of the Africa-Adria margin, a structure referred to as the External Thrust System (Bianchi et al., 1987). This latter undeformed foreland domain forms the southeastern corner of Sicily, the Hyblean Plateau, and is composed of a 25–30 km thick carbonate crust (Lentini et al., 2006). The Hyblean Plateau succession consists of thick Triassic-Liassic carbonate platform with intercalations of mafic volcanics and is overlain by Jurassic-Eocene pelagic carbonates and Tertiary open shelf clastic deposits (Finetti et al., 2005). On the Hyblean Plateau, the exposed sedimentary rocks are mostly of Tertiary up to Quaternary age and it has been the site of intermittent volcanic activity from the Triassic up to the Early Pleistocene. The northern margin of the Hyblean foreland is downthrown by a system of NE-SW oriented normal faults delimiting the Gela-Catania foredeep, which is filled by the allochthonous units of the front wedge of the AMC, the Gela nappe. Borehole data have detected the carbonate succession of the Hyblean foreland in the Catania plain below the foredeep sediments (Torelli et al., 1998). The northward extent of the carbonate bodies (i.e., the External Thrust System) connected to the successions of the Hyblean foreland have been recognised below the roof thrust system of the AMC in northeastern Sicily, as far as the northern flank of Mt Etna (Cristofolini et al., 1979; Bianchi et al., 1987; Branca et al., 2011).

2.2. The sedimentary successions under Mt Etna volcano

Mt Etna is located beside the Ionian coast of Sicily between the Gela-Catania foredeep and the frontal nappes of the Orogenic belt (Branca et al., 2011) (Fig. 1a). In detail, the northeastern sector of the Mt Etna region consists of the Oligo-Miocene terrigenous covers of the AMC and KCC (Branca and Ferrara, 2013). In contrast, the northwestern sector of Mt Etna is dominated by the AMC tectonic units of the Alpine Tethys basinal sequences, the Sicilide tectonic unit, and the Ionides Tethys basinal successions (comprising the Mt Judica tectonic unit) (Branca et al., 2011). The Sicilide tectonic unit consists of both, varicoloured clays (Argille Scagliose Superiori formation) and

Fig. 1. (a) Geological map of eastern Sicily and Mt Etna volcano (modified from Finetti et al., 2005). Yellow stars indicate sampling locations. (b) North–south cross section showing the inferred crustal structure underneath Mt Etna (modified from Branca et al., 2011). The position of the cross section is indicated on panel (a).

Fig. 2. Field photographs. (a) An outcrop of quartzarenite belonging to the Nicosia-Numidian flysch (Apenninic-Maghrebian Chain, Sicilide). (b) Clay-rich unit of the Argille Scagliose Varicolori (Apenninic-Maghrebian Chain, Sicilide). (c) Photograph of the sampled block, embedded in clay-rich loose matrix, within the clay-rich unit of the Argille Scagliose Varicolori (Apenninic-Maghrebian Chain, Sicilide). (d) Outcrop of quartzarenite, part of the Numidian flysch (Apenninic-Maghrebian Chain, Sicilide). (e) Bedded dolomitic limestone from the Scillato Formation within the Mt Judica unit (Apenninic-Maghrebian, Chain Ionides). (f) Loose matrix of clay-rich material from the Catenanuova Formation within the Mt Judica unit (Apenninic-Maghrebian Chain, Ionides). This loose clay-rich matrix material contains massive blocks of limestone. (g) Outcrop of the upper Mt Climiti Formation bedded limestone (Hyblean foreland). (h) Quarry site of the Priolo Formation (Hyblean foreland). Ridges of massive Hyblean bedded limestone can be seen in the background.

terrigenous turbiditic successions, such as the Numidian, Troina-Tusa, and Mt Soro flysches that form the Nebrodi Mountains in the northwest and southwest sectors of Mt Etna. Southwest of the volcano, the Mt Judica tectonic unit is exposed together with the Neogene terrigenous covers. The Quaternary foredeep succession outcrops to the south of Mt Etna (Branca and Ferrara, 2013). On the whole, according to the reconstructed geological crustal section of eastern Sicily of Branca et al. (2011), the AMC allochthonous tectonic units of the Alpine Tethys and the Ionides Tethys form about 3–6 km of the crust beneath Mt Etna (Fig. 1b) and overlie the deformed carbonates (i.e., the ETS) of the African continental margin. These units were thus the target of our sampling campaign.

3. Field campaign and outcrop description

We collected twelve blocks (about 30 × 30 × 30 cm) from the sedimentary basement of Mt Etna: Nine samples were sourced from the Apenninic-Maghrebian Chain, which is subdivided into Sicilide and Ionides sequences, and three samples were sourced from the Hyblean Plateau. All of the collection sites are indicated in Fig. 1a and the lithology of the units sampled and sampling coordinates are summarised in Table 1.

The Sicilide group, heavily deformed by the previous tectonic movements common to this orogeny (Bianchi et al., 1987), is mainly composed of loose clay and therein embedded layers and blocks of marly limestone and quartzarenite (e.g., Fig. 2c). We sampled two blocks of

Table 2
Sample description and petrographic features. "Lithology sampled" gives the rock name. "Outcrop" describes the appearance of the sampled lithology. "Fraction of total deposit" gives the volume percentage of the sampled lithology within the entire unit, e.g., for sample sETNA-01, layers of marly limestone comprise about 30 vol% of the entire unit, the remaining part consisting of unconsolidated material. "Sample description" refers to features observed in hand-specimen or under the binocular using a crushed sample. "Maximum pore diameter", "Maximum grain size", "Fractures", "Veins" and "Bedding" have been constrained under the optical microscope. The column "Texture class" shows the assigned textural classification.

Sample#	Lithology sampled	Outcrop	Fraction of total deposit [vol%]	Sample description (macroscopic/binocular)	Maximum pore diameter [μm]	Maximum grain size [μm]	Fractures	Veins	Bedding	Texture class
sETNA-01	Marly limestone	Layers embedded in clay matrix	30	Homogeneous; mid-grey; clay-bearing, HCl positive	20	30	yes	yes	yes	Micaceous arenite
sETNA-02	Quartzarenite	Massive	40	Heterogeneous; light yellow; qz, HCl negative	500	500	no	no	no	Quartzarenite (rounded)
sETNA-03	Quartzarenite	Sheared and fractured clasts, embedded in clay matrix	90	Homogeneous; dark grey; HCl subdued	2	50	no	no	cross	Quartzarenite (angular)
sETNA-04	Quartzarenite	Sheared and fractured clasts, embedded in clay matrix	80	Heterogeneous; yellow-reddish; white mica; qz; HCl negative	10	100	no	no	yes	Quartzarenite (angular)
sETNA-05	Quartzarenite	Massive	40	Heterogeneous; yellow; <25% qz; HCl negative	1600	700	no	no	no	Quartzarenite (rounded)
sETNA-06	Dolomitic limestone	Massive	100	Homogeneous; grey; HCl positive	2	800	yes	no	yes	Calcarenite (no macropores)
sETNA-07	Radiolaritic limestone	Sheared and fractured clasts, embedded in clay matrix	100	Homogenous; dull, red grains; HCl positive	2	150	yes	no	yes	Radiolarite-bearing limestone
sETNA-08	Marly clay	Loose material	80	Heterogeneous; brown; clay bearing; lithology is loose material (not solidified); HCl positive	n/a	n/a	n/a	n/a	n/a	n/a
sETNA-09	Calcarenite	Massive	100	Homogenous; white; HCl positive	200	400	no	no	yes	Calcarenite (with macropores)
sETNA-10	Calcarenite	Massive	100	Homogenous; bright, slight yellowish; shells; HCl positive	600	800	no	no	yes	Calcarenite (no macropores)
sETNA-11	Limestone	Massive	100	Homogeneous; white; HCl positive	2000	600	no	no	no	Calcarenite (with macropores)
sETNA-12	Marly limestone	Layers embedded in clay matrix (alternative layer to sETNA-01)	30	Homogeneous; grey; HCl positive	2	30	yes	no	yes	Micaceous arenite
ML	Marly limestone		100	Heterogeneous; ocre; HCl subdued	50	50	yes	Yes	yes	Quartzarenite (angular)

marly limestone from the Troina-Tusa flysch (sETNA-01 and 12) and four blocks of quartzarenite, two from the Numidian flysch (sETNA-02, shown in Fig. 2a, and sETNA-05 shown in Fig. 2d), one from the Argille Scagliose Superiori (sETNA-03, shown in Fig. 2b,c), and one from the Mt Soro flysch (sETNA-04) (Table 1). Volumetrically, the marly limestone blocks represented about 30% of the total volume of the Troina-Tusa flysch (with about 70% loose clay matrix). The volume of quartzarenites within the Numidian flysch, Argille Scagliose Superiori, and Mt Soro flysch units ranged from 10 to 80% (Table 2).

For the Ionides group, underlying the Sicilide, we sampled a massive dolomitic limestone from the Mt Judica Scillato Formation (sETNA-06, shown in Fig. 2e), and a radiolaritic limestone from the Mt Judica Crisanti Formation (sETNA-07). This radiolaritic limestone occurs as blocks and fragments in a clay-rich matrix (comparable to the Sicilide lithologies). A representative sample of this clay-rich, loose matrix was taken from the Mt Judica Catenanuova Formation (sETNA-08, shown in Fig. 2f).

The three remaining blocks were sampled from the Hyblean Plateau, which underlies the Ionides sequence. We sampled the upper (sETNA-09) and lower (sETNA-10, Fig. 2g) Mt Climiti Formation and the Priolo Formation (sETNA-11, Fig. 2h). All three units are massive beds of limestone and composed of carbonate shell fragments.

We augmented our sample suite with a sample of the marly limestone (ML) from Mollo et al. (2011). This sample belongs to the Polizzi Formation (Sicilide Unit) of the AMC.

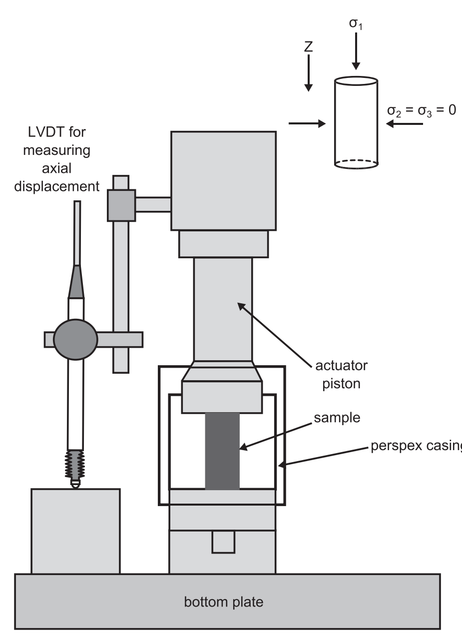

Fig. 3. Schematic diagram of the experimental arrangement used for the uniaxial compressive strength experiments at the Université de Strasbourg (not to scale).

4. Laboratory methods

4.1. Sample preparation

Representative pieces (about 50 g) of each block collected were crushed and powdered (to below 5 μm) for X-ray diffraction analysis (XRD). The rock physical and mechanical properties were measured on cylindrical samples cored from each of the blocks. Cylindrical samples were cored to a diameter of 20 mm and cut and ground flat and parallel to a nominal length of 40 mm. Samples of each block were cored perpendicular to any observable bedding. The samples were dried in an oven at 90 °C for at least 48 h and then in a vacuum oven at 40 °C for 12 h prior to measurement.

4.2. Optical microscopic analysis

The textural and microstructural analysis of each block was performed using a Leica DM2500 microscope with a mounted 5 megapixel Leica DFC425 digital camera using thin sections prepared with blue epoxy. All images were collected using transmitted light.

4.3. X-ray diffractometry (XRD)

The mineral composition was determined at Technische Universität München (TUM), Germany, using XRD analysis. The powdered samples (about 1 g) were mixed with 10% ZnO as an internal standard. Samples were then ground for 8 minutes with 10 ml of isopropyl alcohol in a McCrone Micronising Mill using agate cylinder elements. The analyses were performed on powder mounts using a PW 1800 X-ray diffractometer (CuKα, graphite monochromator, 10 mm automatic divergence slit, step-scan 0.02° 2θ increments per second, counting time 1 s per increment, 40 mA, 40 kV). The crystalline and amorphous phases in the whole rock powders were quantified using the Rietveld program BGMN (Bergmann et al., 1998).

4.4. Porosity measurements

Connected porosity was measured in-house at LMU for each cylindrical core sample using an Ultrapyc helium pycnometer. Measurements were collected using a running pressure of 18 psi, and typically 5 runs per core were performed, 3 of which were taken for calculation of an average. In general, standard deviation values below 0.06 cm^3 were achieved. Following our unconfined compressive strength (UCS) tests (see Section 4.5), the remaining pieces of the sample cores were powdered for total porosity measurements. Samples were ground to a particle size lower than 5 μm to access all of the isolated pores; the volumes of the powders were then measured using the same Ultrapyc helium pycnometer to give the total porosity. The isolated porosity can then be obtained by simply subtracting the connected porosity from the total porosity.

4.5. Benchtop P-wave velocity measurements

The P-wave velocity of the core samples was measured at the Université de Strasbourg using a device coupling: (1) a digital oscilloscope (Agilent Technologies DSO5012A digital storage oscilloscope), (2) a waveform pulse generator (Agilent Technologies 33210A, 10 MHz function/waveform generator), (3) two piezoelectric transducers, located within steel endcaps at the top and bottom of the sample, with a resonant frequency up to 1 MHz, (4) a load cell, and (5) a signal amplifier. All measurements were collected under an axial force of 300 N (to ensure a good contact between the endcaps and the sample) using a 10 volt, 700 kHz input signal. Measurements were collected under ambient laboratory pressure and temperature.

4.6. Uniaxial compressive strength (UCS) tests

Uniaxial compressive strength (UCS) experiments (i.e., $\sigma_1 > \sigma_2 = \sigma_3$; $\sigma_2 = \sigma_3 = 0$) were performed using a uniaxial press at the Université de Strasbourg (Fig. 3). The cylindrical samples were loaded at a constant strain rate of $1.0 \times 10^{-5}\ s^{-1}$ until failure. The axial shortening (strain) of the samples was measured by an external linear variable differential transducer (LVDT), which monitored the movement of the axial piston relative to the static base plate. The axial force was recorded by a load cell, which was then converted to a stress using the sample radius. Since the maximum stress achievable on our uniaxial setup is about 160 MPa for samples of a diameter of 20 mm, some of the low porosity samples were deformed using a higher load deformation apparatus. In this setup, axial force was recorded by a load cell and axial displacement by an LVDT monitoring the position of the piston relative to the static pressure vessel. All experiments were performed under ambient laboratory pressure and temperature, and values of strain were corrected to account for the compliance within the loading train (frame, piston, endcaps, etc.). Using our stress–strain data we also determined the static Young's modulus, calculated simply as the slope of the stress–strain curve within the perceived elastic portion of each curve.

5. Results

5.1. Petrographic analysis

The textural and microstructural (pore size and shape, and grain size and shape) analysis of each block was performed on thin sections prepared with blue epoxy using an optical microscope. The rock types were first grouped according to their texture. The six textural classes of samples are (1) micaceous arenite (Fig. 4a), (2) bedded, angular-grained quartzarenite without macroporosity (Fig. 4b), (3) macroporous quartzarenite with subrounded grains (Fig. 4c), (4) radiolaritic limestone (Fig. 4d), (5) calcarenites without macroporosity (Fig. 4e), and (6) calcarenites containing macroporosity (Fig. 4f) (Table 2). These textural classes are useful for the interpretation of the petrophysical properties, but are not intended to serve as standard rock classifications.

Fig. 4. Photomicrographs of thin sectioned rocks impregnated in blue-dyed epoxy. (a) Marly limestones of the Troina-Tusa flysch (Apenninic-Maghrebian Chain Sicilide) are characterised by silty matrix, containing mica, quartz, and clay. These samples contain fractures, and one of them (sETNA-01) calcite veins. Texturally, these lithologies are micaceous arenites. (b) Quartzarenites from the Argille Scagliose Superiori (sETNA-03), the Monte Soro flysch (sETNA-04), and the Polizzi Formation (ML). All samples are from the Apenninic-Maghrebian Chain Sicilide and consist of angular clasts that show bedding (in one case cross-bedding) and microporosity. (c) Quartzarenites consisting of subrounded to rounded grains of quartz up to 1000 μm in diameter. Pore sizes (evident from the distribution of blue dyed epoxy) can be as large as 2000 μm. Sample sETNA-02 is from the Nicosia-Numidian flysch and sample sETNA-05 from the Numidian flysch (both from the Apenninic-Maghrebian Chain Sicilide). (d) Radiolarian-bearing limestone from the Crisanti Formation (Mt Judica unit, Apenninic-Maghrebian Chain Ionides) that contains a fine-grained matrix embedded with silicic and carbonatic clasts/grains (typically 50–100 μm in diameter). These samples also contain faint bedding and fracturing. Also embedded are microfossils of silicic and carbonatic composition. (e) Calcarenites without macroporosity that consist of biogenic fossils and fossil fragments of up to 1000 μm in size embedded within a fine-grained matrix. Sample sETNA-06 from the Scillato Formation (Mt Judica unit, Apenninic-Maghrebian Chain Ionides) is shown in the left and sample sETNA-10 from the Mt Climiti Formation (Hyblean foreland) in the right. (f) Calcarenites containing macroporosity consist of clast-supported biogenic material and fragments. Sample sETNA-09 from the Mt Climiti Formation on the left and sample sETNA-11 from the Priolo Formation on the right (both from the Hyblean foreland). (g) Microporosity observed in single calcite grains of sample sETNA-11.

As a result, we present both the lithology name and the texture class in Table 2. In the following text we correlate the mineralogical names with their textural classes and provide a brief petrographic description highlighting the important features of each lithology. A summary of petrographic features of each lithology is given in Table 2.

5.1.1. Sicilide

The marly limestones of the Troina-Tusa flysch within the Apenninic-Maghrebian Chain have a matrix particle size within the silt fraction and contain fragments of up to 30 μm. Both marly limestones do not contain macroscopic pores, but contain fractures

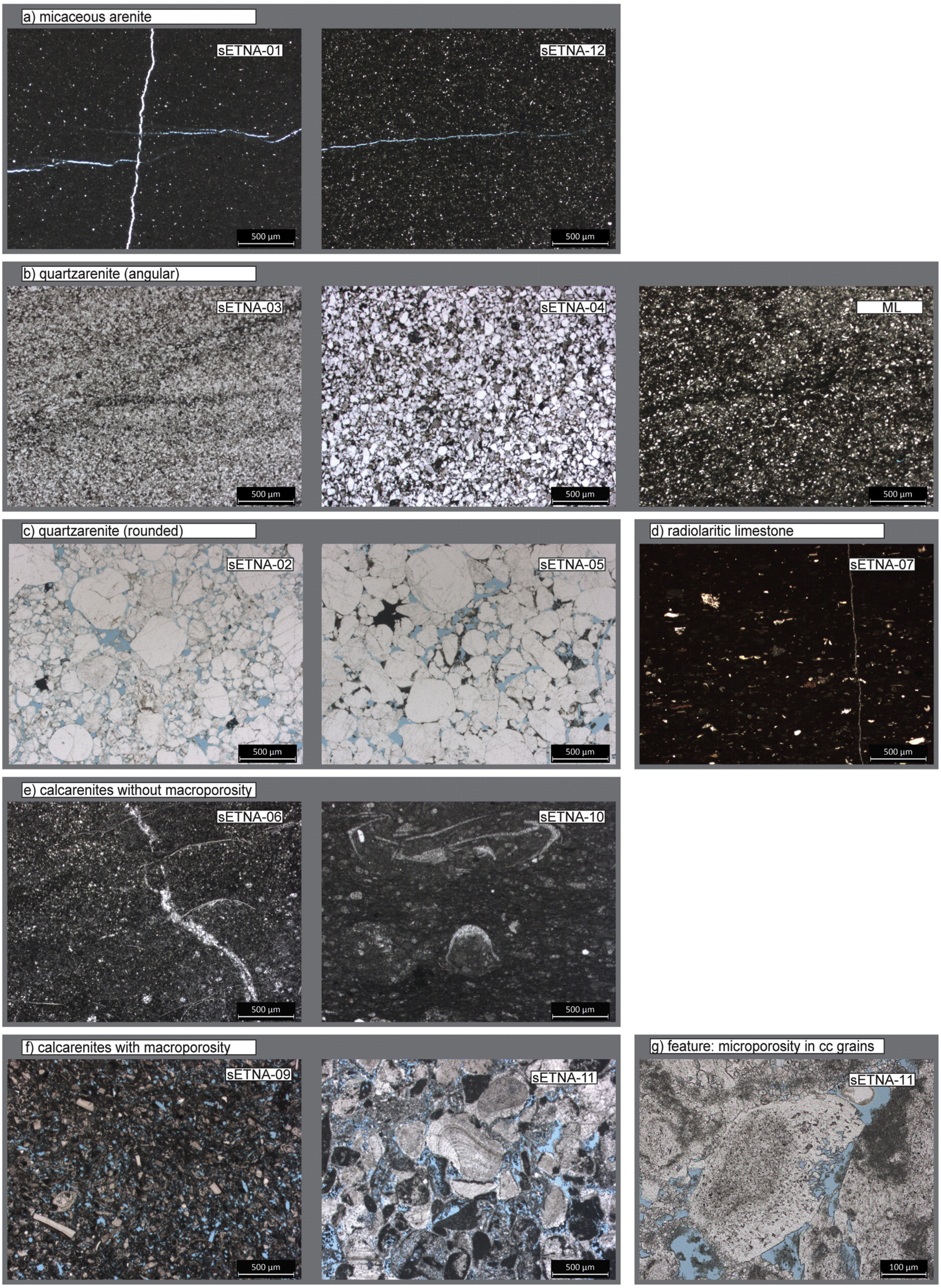

and calcite veins. These marly limestones are classified texturally as micaceous arenites (Fig. 4a). The quartzarenites of the Apenninic-Maghrebian Chain can be texturally split into two subgroups, two lithologies composed of small (20 μm) angular grains that contain grain-scale bedding and cross-bedding features (Fig. 4b) and two lithologies composed of larger (500 μm) subrounded grains (Fig. 4c). The sample ML from the Polizzi Formation, which has been included for comparative reasons, also classifies as quartzarenite of angular grains (Fig. 4b). The fine-grained quartzarenites do not contain macropores (Fig. 4b), while the coarse-grained quartzarenites contain macropores up to 2 mm in diameter (Fig. 4c).

5.1.2. Ionides

The radiolaritic limestone from the Mt Judica Crisanti Formation is composed of a silty matrix, in which abundant angular grains/fragments and microfossils (<150 μm) are embedded. The sample is bedded and fractured (Fig. 4d). The dolomitic limestone of the Mt Judica Scillato Formation contains abundant shell fragments and is texturally classified as calcarenite (i.e., the grain diameter is lower than 2 mm) without macropores (Fig. 4e, sETNA-06). We also note that the sample contains fractures and subtle bedding.

5.1.3. Hyblean plateau

Upper and lower Mt Climiti Formation comprise calcarenites, one with (Fig. 4f, sETNA-09) and one without (Fig. 4e, sETNA-10) macroporosity. The sample from the Priolo Formation is a calcarenite with macroporosity (Fig. 4f, sETNA-11). All three calcarenites (grain size < 2 mm) contain grains of biogenic origin. Larger (>2 mm) shell fragments are scarce.

In several of our samples, fossils or fossil fragments can be found, predominantly bivalves and microfossils such as foraminiferas and radiolarites. The rock samples containing fossils are sETNA-06 and sETNA-07 from the Mt. Judica Formation, and sETNA-09, −10 and −11 from the Hyblean foreland. Please refer to Catalano et al. (1991), Finetti et al. (2005), and Branca et al. (2011) for a more detailed description of the fossils within these lithologies.

5.2. Mineralogical composition

The mineral composition of each block (including the ML sample from Mollo et al. (2011)), as determined by XRD, is presented in Table 3. The dominant phases of the sample suite are calcite and quartz and, in one case, dolomite.

In the Sicilide sequence, quartzarenites range from being purely composed of quartz (sETNA-02 and sETNA-05 contain 98 and 100% quartz, respectively) to assemblages of quartz, albitic feldspar, chlorite, and mica. Sample sETNA-03 contains 68% quartz and features 14% chlorite, 8% feldspar, and 6% mica, while sETNA-04 contains 89% quartz and about 10% albitic feldspar. The marly limestones both have a phase assemblage of calcite, quartz, muscovite, chlorite, and feldspar. Of these two samples, sETNA-01 contains 67% calcite and around 10% of quartz, muscovite/illite, chlorite, and feldspar, whereas sample sETNA-12 contains 44% calcite with 27% of muscovite/illite, 18% quartz, 6% chlorite, and 4% feldspar. Sample ML was found to contain 38% dolomite, 25% quartz, 23% calcite, 8% chlorite, and 3% of both muscovite/illite and albite/plagioclase.

In the Ionides sequence, the dolomitic limestone, sETNA-06, contains 67% calcite, 30% dolomite, and 3% quartz. The radiolaritic limestone, sETNA-07, consists of 53% calcite, 41% quartz, and 6% kaolinite. In this sample, the traces of hematite are responsible for the red colour of this rock. The sample of loose clay-rich material, sETNA-08, taken to be representative of the matrix of the non-massive units (see Table 2), consists of a wide variety of mineral phases, namely 35% quartz, 30% interstratified illite-smectite, 29% kaolinite, about 5% calcite, and accessory anatase and gypsum.

The calcarenites from the Hyblean plateau sETNA-09, −10 and −11 are almost purely calcitic, with subordinate quantities of quartz (<1%).

Table 3
Mineralogical composition of sedimentary units underneath Mt Etna investigated in this study.

Mineral	sETNA-01		sETNA-02		sETNA-03		sETNA-04		sETNA-05		sETNA-06		sETNA-07		sETNA-08		sETNA-09		sETNA-10		sETNA-11		sETNA-12		ML	
Calcite	67	±3	<0.2		3	±1					67	±3	53	±3	4.8	±1	99.5	±0.5	99.8	±0.5	100	±0.2	44.1	±2	23	±2
Dolomite											30	±2													38	±2
Quarz	10	±1	98	±0.5	68	±3	88.6	±1	100		3	±1	41	±2	35	±3	0.5	±0.2	0.2	±0.2	<0.1		18	±1	25	±2
Muscovite/Illite	11	±2	<0.5		6.3	±1	1.3	±0.2															27	±3	3	±2
Chlorite	11	±2			14	±3																	6.5	±2	8	±2
R0 Illite-Smectite															30	±3										
Kaolinite			1.1	±0.2									6	±3	29	±3										
Albite/Plagioclase	1	±0.5	<0.5		8	±2	9.6	±2															4.4	±2	3	±1
Microcline			0.9	±0.2																						
Anatase							0.5	±0.2							0.5	±0.2										
Hematite													<0.5													
Pyrite					<0.5																					
Gypsum					1	±0.2									0.7	±0.2										

5.3. Porosity

The connected, isolated, and total porosity for each core sample is given in Table 4. We find that the total porosity of our samples varies from about 6% up to about 18%. The microstructural complexity of some of the rocks is highlighted by their large volumes (up to 7% in some cases) of isolated porosity. Pores are the main contributor to the porosity of the samples, although we note that some of the samples contain fractures (e.g., Fig. 4a, d). The pores range from a few μm in the case of the fine-grained samples (e.g., Fig. 4d), to almost 2000 μm in the case of the coarse-grained samples (e.g., Fig. 4f, sETNA-11). We also note the presence of microporosity within calcite grains in some of the samples (e.g., Fig. 4g).

5.4. P-wave velocity

The P-wave velocity of our sample suite displays a wide range, from about 2.6 to about 5.8 km.s^{-1} (Table 4). P-wave velocity is plotted against total porosity in Fig. 5a and shows that, globally, P-wave velocity decreases as total porosity increases. In detail, two distinct trends with a different slope are visible, both of which span the entire range of porosities found in our sample suite. In the upper trend, the P-wave velocity decreases from about 6 to 5 kms^{-1} with increasing porosity. In the lower trend, P-wave velocity decreases from 5 to 3 kms^{-1} with increasing porosity.

5.5. Uniaxial compressive strength (UCS)

Representative stress–strain curves for three of the samples are presented as Fig. 6. The curves are initially upward concave, followed by a quasi-linear elastic stage. The curves then show a strain hardening stage before reaching a peak stress (σ_p). Finally, the rock succumbs to macroscopic sample failure, marked by a stress drop. Macroscopic sample failure was typically manifest as an axial split (see Fig. 6 inset). The stress–strain curves are typical of those for rock in compression (e.g., Hoek and Bieniawski, 1965; Brace et al., 1966; Scholz, 1968). We selected to show the three samples in Fig. 6 (the weakest sample, the strongest sample, and a sample of mid-strength) to best display the variability in strength and mechanical behaviour of our sample set. The uniaxial compressive strengths (UCS or σ_p) of all of our samples are summarised in a plot of UCS versus porosity in Fig. 5b; the data are also available in Table 4. The general trend is that UCS decreases 20 fold (from ~13 MPa to ~270 MPa) as total porosity increases (Fig. 5b).

5.6. Static Young's modulus

The static Young's moduli of our samples, calculated from the elastic portion of their stress–strain curves, are plotted against total porosity in Fig. 5c. We observe that Young's modulus decreases as total porosity increases. Young's modulus varies by about an order of magnitude, from about 4.4 GPa to about 45 GPa.

6. Discussion

6.1. P-wave velocity and static Young's modulus

Our data show that, globally, P-wave velocity (Fig. 5a) and static Young's modulus (Fig. 5c) increase as total porosity decreases. These trends have been previously observed for sedimentary rocks (Chang

Table 4
Rock physical properties of each of the 36 cylindrical cores prepared from blocks collected from the sedimentary units underneath Mt Etna for this study. UCS – uniaxial compressive strength; *Vp* – P-wave velocity; *E* – static Young's modulus.

Sample#	Core#	Bulk density [g/cm^3]	Total porosity [vol.%]	Connected porosity [vol.%]	Isolated porosity [vol.%]	UCS [MPa]	V_P [km/s]	E [GPa]
sETNA-01	a	2.50	11.87	4.33	7.54	80.6	3.54	15.58
	b	2.48	12.54	5.24	7.29	71.2	3.61	15.45
	c	2.50	11.68	4.31	7.38	109.4	3.67	15.63
sETNA-02	a	2.19	18.02	17.50	0.52		3.09	
	b	2.22	17.11	16.81	0.31	28.4	3.20	9.87
	c	2.26	15.37	14.98	0.40	13.3	3.52	4.37
	d	2.24	16.28	15.87	0.41	9.89	2.79	4.39
	e	2.26	15.55	16.29	<0.1	18.4	3.12	7.46
sETNA-03	a	2.43	12.17	8.68	3.49			
	b	2.39	13.44	11.83	1.60		3.54	
	c	2.40	13.30	11.76	1.54			
sETNA-04	a	2.35	14.23	13.06	1.18	115.9	3.66	18.26
	b	2.33	15.06	13.79	1.27	99.6	3.67	18.04
	c	2.36	14.12	12.68	1.43	98.5	3.70	18.54
sETNA-05	a	2.35	11.89	12.24	<0.1	118.6	3.70	34.79
	b	2.33	12.93	9.83	3.10	108.2	3.54	31.58
	c	2.34	12.52	11.16	1.36	87.9	3.49	27.96
sETNA-06	a	2.62	6.51	2.19	4.31	130	5.60	43.42
	b	2.63	6.35	1.26	5.08		4.71	
	c	2.61	7.02	4.06	2.96	111.5	4.83	29.63
sETNA-07	a	2.54	6.18	1.42	4.76		4.76	40.24
	b	2.54	6.20	1.46	4.74	270.2	4.79	45.32
	c	2.47	8.73	4.31	4.41	191.8	4.45	32.45
sETNA-09	a	2.49	9.28	4.68	4.60	159.7	5.64	44.54
	b	2.29	16.58	14.96	1.62	59.6	5.21	26.39
	c	2.39	12.83	10.82	2.01	84.5	5.30	29.25
sETNA-10	a	2.38	12.59	9.86	2.74	42.3	5.76	24.85
	b	2.45	10.03	6.91	3.12	41.9	5.70	26.9
	c	2.43	10.79	7.54	3.26		5.67	
sETNA-11	a	2.24	17.99	16.37	1.62	34.9	5.27	21.87
	b	2.23	18.55	17.25	1.31	27.3	4.93	17.06
	c	2.25	17.59	16.28	1.31	41	4.89	23.5
sETNA-12	a	2.44	12.00	10.71	1.29			
	b	2.44	11.90	10.47	1.42	65.4	2.57	5.89
ML	a	2.61	7.51	7.17	0.34	73.4	4.64	18.63
	b	2.58	8.44	8.63	<0.1	71.3	5.06	30.94

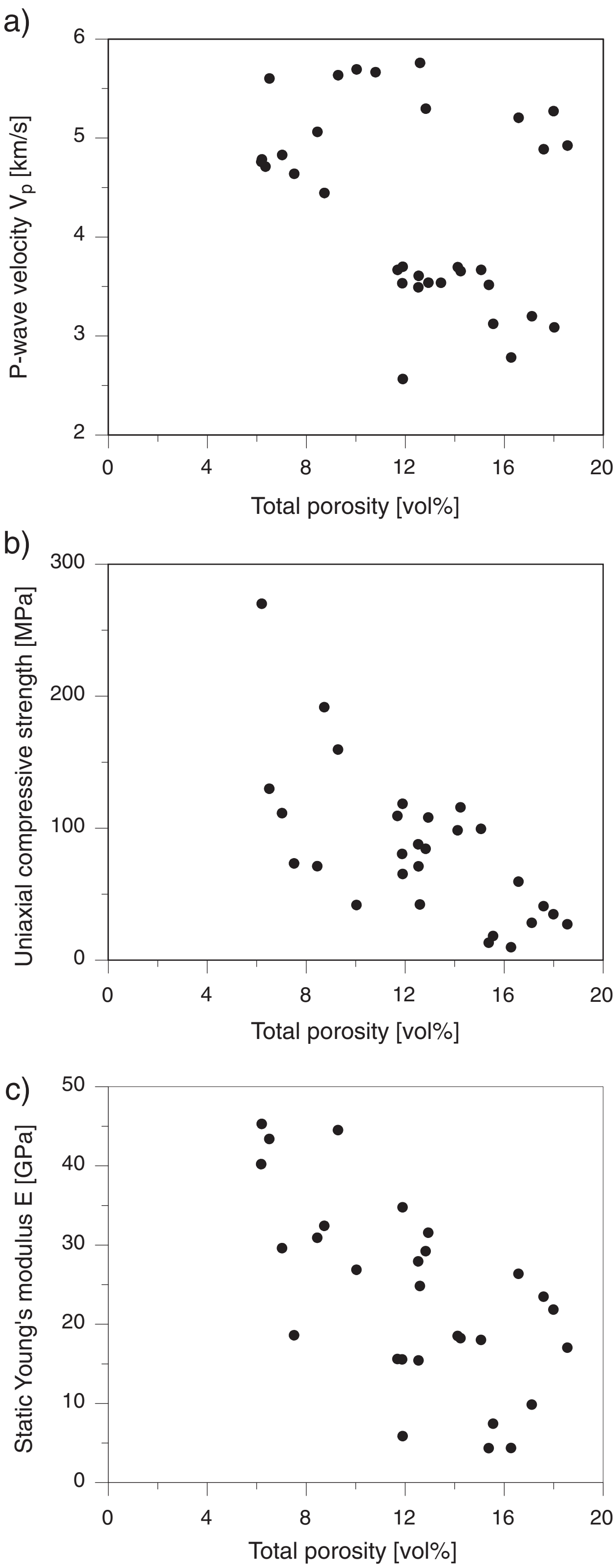

Fig. 5. Physical property data. (a) P-wave velocity (*Vp*) against total porosity. (b) Uniaxial compressive strength (peak stress) against total porosity. (c) Static Young's modulus (tangent modulus) against total porosity.

et al., 2006 and references therein). To better understand these data, we have grouped them by their main mineral phase: calcite, quartz, calcite/quartz, or calcite/quartz/muscovite (Fig. 7).

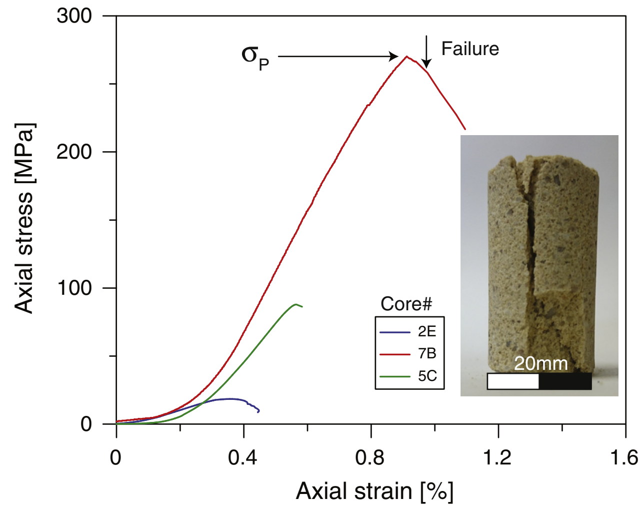

Fig. 6. Representative stress–strain curves from our experimental campaign. The inset shows the typical sample failure mode (axial splitting). Stress–strain curves chosen are the samples with the highest and the lowest peak strength, and a sample with an intermediate peak strength.

We observe no correlation between Young's modulus and the main mineral phase (Fig. 7a). Young's modulus increases as porosity decreases for all of the groups (although we note that only one sample exists for the calcite/quartz/muscovite group). We can conclude that porosity, rather than the most abundant mineral phase, appears to control the Young's modulus of the samples collected.

By contrast, our P-wave velocity data appear to be influenced by the main mineral phase of the rock (Fig. 7b). Of the two distinct trends identified previously (see Section 5.4), we notice that the upper trend, which decreases from about 6 to 5 kms^{-1} over a porosity range of 6 to 18%, is composed entirely of purely carbonatic rocks from the Hyblean plateau. The lower trend is composed of rocks from the quartz, calcite/quartz, and calcite/quartz/muscovite groups, together with a few samples from the calcite group. Since the calcite-pure rocks of the Hyblean foreland contain a wide variety of grain and pore sizes (Fig. 4), it is likely that the high P-wave velocities of these rocks can be largely explained by the higher P-wave velocity of calcite ($V_p = 6.65$ kms^{-1}; Guéguen and Palciauskas, 1994) with respect to quartz ($V_p = 6.06$ kms^{-1}; Guéguen and Palciauskas, 1994). We therefore conclude that the main mineral phase, as well as the total porosity, exerts a control on the P-wave velocity of the sedimentary rocks beneath Mt Etna volcano.

6.2. Uniaxial compressive strength (UCS)

The strength of sub-Etnean sedimentary lithologies decreases with increasing porosity (Fig. 5b). This behaviour is consistent with previous findings on the relationship between porosity and peak strength (e.g. Paterson and Wong, 2005; Chang et al., 2006; Baud et al., 2014; Heap et al., 2014).

To better understand the observed variation in strength we have deployed the micromechanical model of Sammis and Ashby (1986). The pore-emanating crack model of Sammis and Ashby (1986) has been previously, and successfully, used to describe the mechanical behaviour of limestones (e.g., Zhu et al., 2010) and sandstones (e.g., Baud et al., 2014).

The pore-emanating crack model of Sammis and Ashby (1986) describes a two-dimensional elastic medium populated by circular holes of uniform radius *r*. As the applied stress increases, cracks emanate from the circular holes (parallel to the direction of the applied stress) when the stress at the tip of a small crack on the circular surface reaches a critical value (K_{IC}, the fracture toughness). The newly-formed cracks propagate to a distance *l* in the direction of the maximum principal stress. Once the cracks are long enough they can interact, thus increasing the local tensile stress intensity. Eventually, they coalesce and

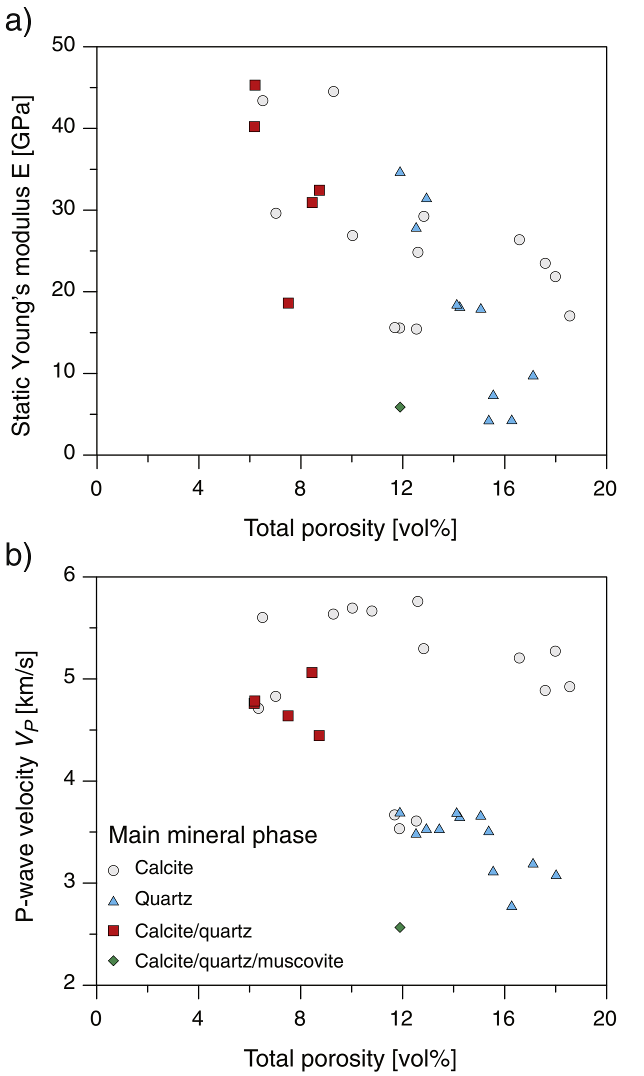

Fig. 7. (a) Static Young's modulus versus total porosity. Data are grouped according to their main mineral phase (calcite, quartz, calcite/quartz, or calcite/quartz/muscovite). (b) P-wave velocity versus total porosity. Data are grouped according to their main mineral phase (calcite, quartz, calcite/quartz, or calcite/quartz/muscovite).

conspire to induce the macroscopic failure of the elastic medium. In the case of uniaxial compression, Zhu et al. (2010) derived an analytical approximation of Sammis and Ashby's (1986) pore-emanating crack model to estimate UCS ($\sigma_{p,}$ the peak stress) as a function of the bulk sample porosity (φ):

$$\sigma_p = \frac{1.325}{\varphi^{0.414}} \frac{K_{IC}}{\sqrt{\pi r}}$$

The analytical solution has two microstructural terms: the fracture toughness (K_{IC}) and the pore radius. Since the materials analysed in this study are a mix of carbonates and sandstones ($K_{IC} = 0.2$ MPa.m$^{0.5}$ for calcite and $K_{IC} = 1.0$ MPa.m$^{0.5}$ for quartz; Atkinson and Meredith, 1987) and contain a range of pore sizes (from a few μm up to about one mm), our data cannot be described by a single modelled curve. However, it is still possible, using the model, to glean information about the factors controlling the mechanical behaviour of the sample materials.

We will first consider pore size. In the graph of peak stress (σ_p) versus total porosity, presented as Fig. 8a, we have grouped the data points into two categories: Those rocks with a pore diameter less than 50 μm and those with a pore diameter more than 200 μm. Firstly, we note that the weakest samples in our dataset also contain the largest pores, even those with a porosity comparable to the samples with smaller pore diameters. If we employ the pore-emanating crack model to try to capture the behaviour of the samples with the large pores (solid curve on Fig. 8a), we see that, using a fixed pore size of 300 μm, the fracture toughness predicted by the model is 3.45 MPa.m$^{0.5}$. However, the experimentally derived values of K_{IC} for calcite and quartz, the main constituents of the samples, are significantly lower than this value: 0.2 and 1.0 MPa.m$^{0.5}$, respectively (Atkinson and Meredith, 1987). We highlight that increasing the pore size (some of the samples within the > 200 μm group contain pores up to 2000 μm in diameter) only serves to further increase the fracture toughness required to describe the dataset. This analysis suggests that, although pore size may play an important role, it is not the only factor dictating the strength of the materials tested.

We will now consider mineralogical composition. Fig. 8b shows the peak stress (σ_p) against total porosity, however, this time, we have classified each sample based on their major mineral constituents. On first inspection, there appears to be no link between the strength of the samples and their mineralogical composition, the samples containing mostly calcite or mostly quartz cover a very similar range of porosities and strengths. Further, the Sammis and Ashby (1986) micromechanical model shows that each group cannot be described by a single curve, best observed in our quartz-rich materials. Using a fixed value of K_{IC} (of 1.0 MPa.m$^{0.5}$ for quartz), we show that the data for our quartz-rich rocks require two modelled curves, one assuming a pore diameter of 600 μm and one assuming a pore diameter of 10 μm (Fig. 8b). While the estimation of a 600 μm pore size for the more porous (15–17%) group of quartz-rich materials is in agreement with our microstructural observations (Fig. 4), the less porous (12–15%) group, for which the model assumes a pore diameter of 10 μm, contains a number of samples with pore sizes greater than 200 μm. This analysis suggests that the strength of the samples is not simply a function of their mineralogical composition.

Finally, we will consider the role of textures on the peak stress (σ_p) vs. total porosity relationship (Fig. 8c). If texture was the principal factor controlling the strength of the rocks we may observe that, regardless of their porosity, samples of the same texture would have a similar strength. This is however not the case. The calcarenites, for instance, vary in strength from 42 MPa to 160 MPa (Fig. 8c).

Other microstructural attributes not considered here, or by the pore-emanating crack model of Sammis and Ashby (1986), include pore shape, grain size and shape, pore and grain size distribution, and the presence of microcracks. Our microstructural observations illustrate that these parameters also vary between the lithologies (Fig. 4). We can conclude that the observed variation in strength is a result of the large variability in microstructural parameters (pore size, mineralogical composition, texture, pore shape, grain size and shape, and pore and grain size distribution, amongst others) between the lithologies, emphasising the extremely variable nature of the sediments that exist beneath Mt Etna.

6.3. Implications for Mt Etna

The experimental strength and P-wave velocity data (collected at ambient pressure and temperature conditions), grouped by stratigraphy (Sicilide, Ionides, or Hyblean plateau), are plotted alongside a schematic cross section of the crustal structure underneath Mt Etna in Fig. 9 (modified from Branca et al., 2011). While we are aware that the values of strength and P-wave velocity will likely change as a function of depth (e.g. Paterson and Wong, 2005), we present the data in this way to investigate whether any trends exist between rock physical properties and depth within the sub-Etnean stratigraphy. Although uniaxial compressive strength (UCS) and P-wave velocity measurements collected under ambient laboratory pressures may not accurately represent the natural case, these methods are nevertheless considered as the "standard" way to assess rock properties, allowing our data to be compared with the wealth of preexisting data. Further, we emphasise that motivation of our study was to investigate the extent of the variability of the sediments below Mt Etna. Our experiments have shown, for example, that the variability in uniaxial compressive strength of the sedimentary lithologies underneath Mt Etna can be as high as a factor of twenty; while the absolute values may differ, we anticipate that a similar *variability* in strength and P-wave velocity may exist at depth. Correlated with tectonostratigraphic position, the relative variability in rock physical properties show some noteworthy features. For instance, deeper positioned lithologies have higher P-wave velocities (Fig. 9a). This is most likely a result of rock type and initial burial conditions, since all the samples measured were collected at atmospheric pressure. However, and as noted above, P-wave velocities are likely to change as pressure and temperature increase with increasing depth. While the increase in pressure is likely to increase P-wave velocities (e.g. Kern et al., 2002), we note that the elevated temperatures expected within these sedimentary units (e.g., Lundgren et al., 2004; Del Negro et al., 2009; Bonaccorso et al., 2010) may act to decrease P-wave velocity through dehydroxylation and decarbonation reactions (Mollo et al., 2011; Heap et al., 2013) and thermal microcracking (Mollo et al., 2012, 2013). We further highlight that P-wave velocities are often higher when rock is saturated with a fluid phase (O'Connell and Budiansky, 1974); our P-wave velocity data were collected on dry rock samples.

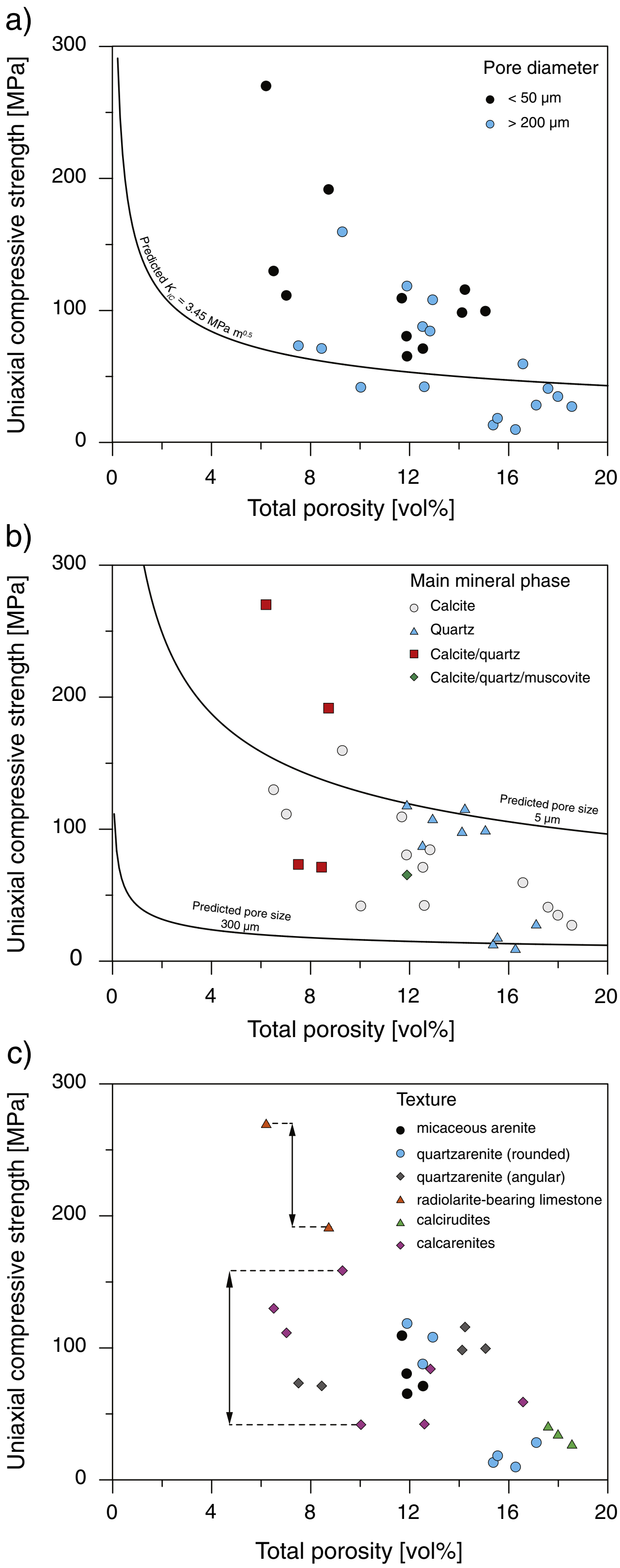

In contrast to the P-wave velocity data, the UCS data show less systematic variations with respect to the tectonostratigraphic setting (Fig. 9b). For example, the weakest rocks are found in the Sicilide, the uppermost sequence of the Etna basement. This is however consistent with inferred depth of zones of weakness, which may contribute to large-scale sliding of the eastern flank Mt Etna (e.g., Bonforte and Puglisi, 2006). Below the Sicilide, the units of the Ionides sequence exhibit the highest values of UCS. The deepest units, those of the Hyblean plateau, were found to be weaker than those of the Ionides sequence. However, we note that the pressure and temperature (e.g., Lundgren et al., 2004; Del Negro et al., 2009; Bonaccorso et al., 2010) conditions at depths relevant for the Hyblean plateau are likely to encourage ductile behaviour (e.g. Heap et al., 2013). In the brittle regime, an increase in temperature is also likely to reduce the strength of limestone. For example, the strength of Solnhofen limestone at an effective pressure of 50 MPa was reduced from 360 MPa at room temperature to 306 MPa at a temperature of 200 °C (Xiao et al., 2003). Further, the presence of a fluid phase may also influence the strength of the suite of rocks studied herein. The strength of limestone can be reduced through both mechanical (Baud et al., 2009) and chemical effects (Brantut et al., 2014), and significant calcite dissolution can occur in the presence of a CO_2-saturated fluid (Grgic, 2011).

Perhaps most pertinent for the structural stability of the edifice at Mt Etna, our field observations have revealed that some of the units within the AMC (Sicilide and Ionides) are tectonically disaggregated units that contain significant quantities (10–80%) of loose, clay-rich material (see Fig. 2f and Table 2). If one assumes that the weakest layer within a sequence is the most influential in determining the macroscopic strength of a particular unit, results from our field campaign indicate that these clay-rich horizons may be dictating the "effective" strength of the basement underneath Mt Etna. Although such disaggregated material is inappropriate for traditional petrophysical analyses, we can speculate that the strength of these units is likely to be several orders of magnitude lower than some of the more competent rock units (e.g., Byerlee, 1978). However, as for competent units, the properties of such unconsolidated material at depth may differ from what we can sample from surface outcrops. Further, we note that these disaggregated units are extremely clay-rich (sample sETNA-08), containing 30% illite/

Fig. 8. Uniaxial compressive strength against total porosity. (a) Data are grouped based on their pore size (either <50 µm or >200 µm). Solid line is a modelled curve using the micromechanical model of Sammis and Ashby (1986) at a fixed pore size of 300 µm; the best fit to the dataset requires a value of K_{IC} of 3.45 MPa m$^{0.5}$. (b) Data are grouped based on their dominant mineral phase (calcite, quartz, calcite/quartz, or calcite/quartz/muscovite). The modelled curves, again from the micromechanical model of Sammis and Ashby (1986), were designed to pass through the two groups of quartz rocks (blue triangles) using the K_{IC} value of quartz (1.0 MPa m$^{0.5}$, Atkinson and Meredith, 1987). The modelled curves predict pores sizes of either 5 or 300 µm. (c) Data are grouped based on their texture (micaceous arenite, quartzarenite (rounded), quartzarenite (angular), radiolarian-bearing limestone, calcirudites, or calcarenites). We have indicated the maximum difference in strength between samples of the same texture within the radiolarian-bearing limestone and calcarenites classes.

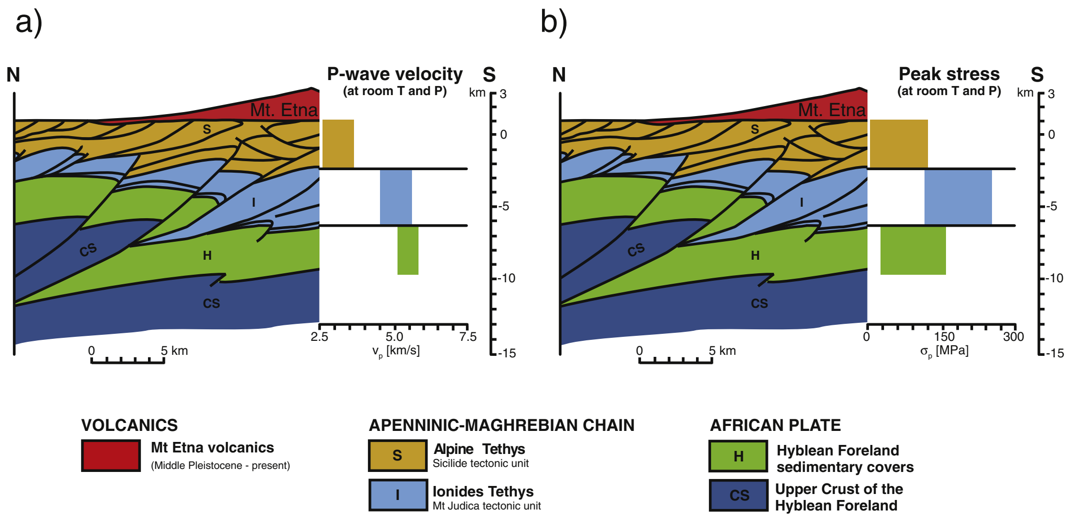

Fig. 9. Variability of experimental data in correlation with stratigraphic position of rock units. a) p-wave velocity and b) uniaxial compressive strength. Note that the data presented have been collected at room temperature and atmospheric pressure and do not reflect the properties at depth in the crust.

smectite and 29% kaolinite (Table 2). We highlight that friction experiments have demonstrated that clay-rich gouges are consistently weak (Ikari et al., 2009). These units may therefore heavily contribute to large-scale deformation or the formation of shear horizons. Inferences of large decollement surfaces underneath Mt Etna (e.g., Borgia et al., 1992, 2000a, b; Froger et al., 2001; Bonforte and Puglisi, 2003; Lundgren et al., 2004; Neri et al., 2004; Rust et al., 2005; Bonforte and Puglisi, 2006; Palano et al., 2008, 2009; Neri et al., 2009) may therefore be related to the presence of such disaggregated, clay-rich horizons.

6.4. Models of edifice stability at Mt Etna

Models dealing with the stability of volcanic edifices require the input of various strength parameters (e.g., Russo et al., 1997; Apuani et al., 2005; Moon et al., 2009; Apuani et al., 2013). Data on the peak stress of intact rock materials are important, for example, to calculate the rock mass values of friction angle, cohesion, and elastic parameters (Hoek et al., 2002), and can thus contribute to the numerical calculation of volcanic edifice stability. Moreover, data on peak stress of lithologies are useful for the geotechnical characterisation of rock units. Rock mass rating (RMR), for instance, is a measure for strength and deformation properties of a rock formation (Singh, 2011), and uniaxial compressive strength is necessary for the calculation of this classification (e.g., Moon et al., 2005). The data produced here are therefore relevant for future studies aiming to constrain the structural stability of Mt Etna.

Our experiments have shown that the variability in uniaxial compressive strength of the sedimentary lithologies underneath Mt Etna can be as high as a factor of twenty. Typically, tensile strength is about a tenth or twelfth of the uniaxial compressive strength (Jaeger et al., 2007). For this reason, we also expect tensile strength, a useful parameter in the calculation of flank stability models (e.g. Apuani et al., 2013), to vary by a factor of about twenty. As a result, the wide heterogeneity in lithologies underneath the volcano may not be aptly described by a single value of strength (compressive or tensile), as is common practice for numerical models. However, although we highlight the challenges for stability modelling at Mt Etna, we are aware that technical limitations may require modellers to derive "effective" strength values for entire rock sequences.

7. Concluding remarks

Our combined field and laboratory study has revealed that the sedimentary basement of Mt Etna is characterised by vast heterogeneity. We find that, although the rocks of the Apenninic-Maghrebian Chain and the Hyblean Plateau are predominantly limestones or sandstones, or a mixture of these two end members, their microstructural attributes and textures vary tremendously. The range of pore and grain size vary by multiple orders of magnitude, and pore and grain shape is highly variable. Further, some samples are characterised by mesoscale bedding or the presence of veins or fractures. This prodigious variety of mineralogical composition, microstructure, and texture has resulted in a wide range of laboratory-measured physical properties. Total porosity varies from 6 to 18%, P-wave velocity from 2.6 to 5.8 kms^{-1}, uniaxial compressive strength from 13 to 270 MPa, and static Young's modulus from 4.4 to 45 GPa. The wide array of parameters controlling the strength of the samples was highlighted by the inability of the pore-emanating crack micromechanical model of Sammis and Ashby (1986) to capture the mechanical behaviour of the samples; a model which typically adequately describes the behaviour of sandstones and limestones. Although our data was collected at ambient pressure and temperature conditions, and therefore their direct use in flank stability models requires further consideration, we emphasise that our study aptly demonstrates the extreme variability of the sub-volcanic basement at Mt Etna and, on this basis, we urge caution when selecting input parameters for models of flank stability.

Acknowledgements

We are grateful for the constructive reviews of Silvio Mollo and Bruno Scaillet. This project was funded by the European MEDiterranean SUpersite Volcanoes (MED-SUV) grant, project task 5.3.6. M. J. Heap also acknowledges a Hubert Curien Partnership (PHC) Procope grant (grant number 332065SG) funded and implemented by the Deutscher Akademischer Austauschdienst (DAAD) in Germany, and the Ministry of Foreign Affairs (MAEDI) and the Ministry of Higher Education and Research (MENESR) in France. D. B. Dingwell acknowledges the ERC advanced grant "EVOKES" (Explosive volcanism in the earth system: experimental insights, project number 247076). Y. Lavallée acknowledges funds from ERC starting grant "SLiM" (Strain localisation in magmas, project number 306488). We are grateful to Thierry Reuschlé for his role in the development and maintenance of the laboratory equipment at the Université de Strasbourg.

References

Acocella, V., Puglisi, G., Amelung, F., 2013. Flank instability, eruptions, seismicity and hazard: the case of Mt Etna. J. Volcanol. Geotherm. Res. 251, 1–4.

Apuani, T., Corazzato, C., Cancelli, A., Tibaldi, A., 2005. Physical and mechanical properties of rock masses at Stromboli: a dataset for volcano instability evaluation. Bull. Eng. Geol. Environ. 64 (4), 419–431.
Apuani, T., Corazzato, C., Merri, A., Tibaldi, A., 2013. Understanding Etna flank instability through numerical models. J. Volcanol. Geotherm. Res. 251, 112–126.
Atkinson, B.K., Meredith, P.G., 1987. Experimental fracture mechanics data for rocks and minerals. In: Atkinson, B.K. (Ed.), Fracture mechanics of rock. Academic Press, London, pp. 477–525.
Baud, P., Vinciguerra, S., David, C., Cavallo, A., Walker, E., Reuschlé, T., 2009. Compaction and failure in high porosity carbonates: Mechanical data and microstructural observations. Pure Appl. Geophys. 166, 869–898.
Baud, P., Wong, T.-f., Zhu, W., 2014. Effects of porosity and crack density on the compressive strength of rocks. Int. J. Rock Mech. Min. Sci. 67 (0), 202–211.
Benson, P.M., Thompson, B.D., Meredith, P.G., Vinciguerra, S., Young, R.P., 2007. Imaging slow failure in triaxially deformed Etna basalt using 3D acoustic-emission location and X-ray computed tomography. Geophys. Res. Lett. 34 (3), L03303.
Bergmann, J., Friedel, P., Kleeberg, R., 1998. BGMN - a new fundamental parameters based Rietveld program for laboratory X-ray sources, it's use in quantitative analysis and structure investigations. Commission of Powder Diffraction, International Union of Crystallography CPD Newsletter. 20 pp. 5–8.
Bianchi, F., Carbone, S., Grasso, M., Invernizzi, G., Lentini, F., Longaretti, G., Merlini, S., Mostardini, F., 1987. Sicilia orientale: profilo geologico Nebrodi-Iblei. Mem. Soc. Geol. Ital. 38, 429–458.
Bonaccorso, A., Currenti, G., Del Negro, C., Boschi, E., 2010. Dike deflection modelling for inferring magma pressure and withdrawal, with application to Etna 2001 case. Earth Planet. Sci. Lett. 293 (1–2), 121–129.
Bonforte, A., Puglisi, G., 2003. Magma uprising and flank dynamics on Mount Etna volcano, studied using GPS data (1994–1995). J. Geophys. Res. Solid Earth 108 (B3), 2153.
Bonforte, A., Puglisi, G., 2006. Dynamics of the eastern flank of Mt. Etna volcano (Italy) investigated by a dense GPS network. J. Volcanol. Geotherm. Res. 153 (3–4), 357–369.
Bonforte, A., Guglielmino, F., Coltelli, M., Ferretti, A., Puglisi, G., 2011. Structural assessment of Mount Etna volcano from Permanent Scatterers analysis. Geochem. Geophys. Geosyst. 12 (2). http://dx.doi.org/10.1029/2010GC003213.
Borgia, A., Ferrari, L., Pasquare, G., 1992. Importance of gravitational spreading in the tectonic and volcanic evolution of Mount Etna. Nature 357 (6375), 231–235.
Borgia, A., Delaney, P.T., Denlinger, R.P., 2000a. Spreading volcanoes. Annu. Rev. Earth Planet. Sci. 28 (1), 539–570.
Borgia, A., Lanari, R., Sansosti, E., Tesauro, M., Berardino, P., Fornaro, G., Neri, M., Murray, J.B., 2000b. Actively growing anticlines beneath catania from the distal motion of Mount Etna's Decollement measured by SAR interferometry and GPS. Geophys. Res. Lett. 27 (20), 3409–3412.
Brace, W.F., Paulding, B.W., Scholz, C., 1966. Dilatancy in the fracture of crystalline rocks. J. Geophys. Res. 71 (16), 3939–3953.
Branca, S., Ferrara, V., 2013. The morphostructural setting of Mount Etna sedimentary basement (Italy): Implications for the geometry and volume of the volcano and its flank instability. Tectonophysics 586, 46–64.
Branca, S., Coltelli, M., Groppelli, G., Lentini, F., 2011. Geological map of Etna volcano, 1: 50,000 scale. Ital. J. Geosci. 130 (3), 265–291.
Brantut, N., Heap, M.J., Baud, P., Meredith, P.G., 2014. Mechanisms of time-dependent deformation in porous limestone. J. Geophys. Res. 119, 5444–5463.
Byerlee, J., 1978. Friction of rocks. Pure Appl. Geophys. 116 (4–5), 615–626.
Catalano, R., Di Stefano, P., Kozur, H., 1991. Permian circum-Pacific deep-water faunas from the western Tethys (Sicily, Italy) - new evidences for the position of the Permian Tethys. Palaeogeogr. Palaeoclimatol. Palaeoecol. 87, 74–108.
Chang, C., Zoback, M.D., Khaksar, A., 2006. Empirical relations between rock strength and physical properties in sedimentary rocks. J. Pet. Sci. Eng. 51 (3–4), 223–237.
Cristofolini, R., Lentini, F., Patanè, D., Rasà, R., 1979. Integrazione di dati geologici, geofisici e petrologici per la stesura di un profilo crostale in corrispondenza dell'Etna. Boll. Soc. Geol. Ital. 98, 239–247.
Del Negro, C., Currenti, G., Scandura, D., 2009. Temperature-dependent viscoelastic modeling of ground deformation: application to Etna volcano during the 1993–1997 inflation period. Phys. Earth Planet. Inter. 172, 299–309.
Finetti, I.R., Lentini, F., Carbone, S., Del Ben, A., Di Stefano, A., Forlin, E., Guarnieri, P., Pipan, M., Prizzona, A., 2005. Geological outline of Sicily and lithospheric tectono-dynamics of its Tyrrhenian Margin from new CROP seismic data. In: Finetti, I.R. (Ed.), CROP Deep Seismic exploration of the Mediterranean Region Special Volume. Elsevier, pp. 319–376.
Fortin, J., Stanchits, S., Vinciguerra, S., Guéguen, Y., 2011. Influence of thermal and mechanical cracks on permeability and elastic wave velocities in a basalt from Mt. Etna volcano subjected to elevated pressure. Tectonophysics 503 (1–2), 60–74.
Froger, J.L., Merle, O., Briole, P., 2001. Active spreading and regional extension at Mount Etna imaged by SAR interferometry. Earth Planet. Sci. Lett. 187 (3–4), 245–258.
Grasso, M., Lentini, F., 1982. Sedimentary and tectonic evolution of the eastern Hyblean Plateau (southeastern Sicily) during late Cretaceous to Quaternary time. Palaeogeogr. Palaeoclimatol. Palaeoecol. 39 (3–4), 261–280.
Grgic, D., 2011. Influence of CO2 on the long-term chemomechanical behavior of an oolitic limestone. J. Geophys. Res. 116 (B7). http://dx.doi.org/10.1029/2010JB008176.
Guéguen, Y., Palciauskas, V., 1994. Introduction to the physics of rocks. Princeton University Press, Princeton, N.J. (304 pp.).
Heap, M.J., Vinciguerra, S., Meredith, P.G., 2009. The evolution of elastic moduli with increasing crack damage during cyclic stressing of a basalt from Mt. Etna volcano. Tectonophysics 471 (1–2), 153–160.
Heap, M.J., Baud, P., Meredith, P.G., Vinciguerra, S., Bell, A.F., Main, I.G., 2011. Brittle creep in basalt and its application to time-dependent volcano deformation. Earth Planet. Sci. Lett. 307 (1–2), 71–82.
Heap, M.J., Mollo, S., Vinciguerra, S., Lavallée, Y., Hess, K.U., Dingwell, D.B., Baud, P., Iezzi, G., 2013. Thermal weakening of the carbonate basement under Mt. Etna volcano (Italy): Implications for volcano instability. J. Volcanol. Geotherm. Res. 250, 42–60.
Heap, M., Xu, T., Chen, C.-f., 2014. The influence of porosity and vesicle size on the brittle strength of volcanic rocks and magma. Bull. Volcanol. 76 (9), 1–15.
Hoek, E., Bienawski, Z.T., 1965. Brittle rock fracture propagation in rock under compression. Int. J. Fract. Mech. 1 (3), 137–155.
Hoek, E., Carranza-Torres, C., Corkum, B., 2002. Hoek-Brown criterion – 2002 edition 1. Proc. NARMS-TAC Conference, Toronto, pp. 267–273.
Ikari, M.J., Saffer, D.M., Marone, C., 2009. Frictional and hydrologic properties of clay-rich fault gouge. J. Geophys. Res. Solid Earth 114 (B5), B05409.
Jaeger, J.C., Cook, N.G.W., Zimmermann, R., 2007. Fundamentals in rock mechanics. Wiley-Blackwell (488 pp.).
Kern, H., Jin, Z., Gao, S., Popp, T., Xu, Z., 2002. Physical properties of ultrahigh-pressure metamorphic rocks from the Sulu terrain, eastern central China: implications for the seismic structure at the Donghai (CCSD) drilling site. Tectonophysics 354 (3–4), 315–330.
Lentini, F., 1982. The geology of the Mt. Etna basement. Mem. Soc. Geol. Ital. 23, 7–25.
Lentini, F., Catalano, S., Carbone, S., 1996. The external thrust system in southern Italy; a target for petroleum exploration. Pet. Geosci. 2 (4), 333–342.
Lentini, F., Carbone, S., Guarnieri, P., 2006. Collisional and postcollisional tectonics of the Apenninic-Maghrebian orogen (southern Italy). Geol. Soc. Am. Spec. Pap. 409, 57–81.
Lundgren, P., Casu, F., Manzo, M., Pepe, A., Berardino, P., Sansosti, E., Lanari, R., 2004. Gravity and magma induced spreading of Mount Etna volcano revealed by satellite radar interferometry. Geophys. Res. Lett. 31 (4), L04602.
Mollo, S., Vinciguerra, S., Iezzi, G., Iarocci, A., Scarlato, P., Heap, M.J., Dingwell, D.B., 2011. Volcanic edifice weakening via devolatilization reactions. Geophys. J. Int. 186 (3), 1073–1077. http://dx.doi.org/10.1111/j.1365-246X.2011.05097.x.
Mollo, S., Heap, M.J., Iezzi, G., Hess, K.-U., Scarlato, P., Dingwell, D.B., 2012. Volcanic edifice weakening via decarbonation: A self-limiting process? Geophys. Res. Lett. 39 (15), L15307.
Mollo, S., Heap, M.J., Dingwell, D.B., Hess, K.U., Iezzi, G., Masotta, M., Scarlato, P., Vinciguerra, S., 2013. Decarbonation and thermal microcracking under magmatic P-T-f CO2 conditions: the role of skarn substrata in promoting volcanic instability. Geophys. J. Int. 195 (1), 369–380.
Moon, V., Bradshaw, J., Smith, R., de Lange, W., 2005. Geotechnical characterisation of stratocone crater wall sequences, White Island Volcano, New Zealand. Eng. Geol. 81 (2), 146–178.
Moon, V., Bradshaw, J., de Lange, W., 2009. Geomorphic development of White Island Volcano based on slope stability modelling. Eng. Geol. 104 (1–2), 16–30.
Neri, M., Acocella, V., Behncke, B., 2004. The role of the Pernicana Fault System in the spreading of Mt. Etna (Italy) during the 2002–2003 eruption. Bull. Volcanol. 66 (5), 417–430.
Neri, M., Casu, F., Acocella, V., Solaro, G., Pepe, S., Berardino, P., Sansosti, E., Caltabiano, T., Lundgren, P., Lanari, R., 2009. Deformation and eruptions at Mt. Etna (Italy): A lesson from 15 years of observations. Geophys. Res. Lett. 36 (2), L02309.
O'Connell, R.J., Budiansky, B., 1974. Seismic velocities in dry and saturated cracked solids. J. Geophys. Res. 79, 5412–5426.
Palano, M., Puglisi, G., Gresta, S., 2008. Ground deformation patterns at Mt. Etna from 1993 to 2000 from joint use of InSAR and GPS techniques. J. Volcanol. Geotherm. Res. 169 (3–4), 99–120.
Palano, M., Gresta, S., Puglisi, G., 2009. Time-dependent deformation of the eastern flank of Mt. Etna: After-slip or viscoelastic relaxation? Tectonophysics 473 (3–4), 300–311.
Paterson, M.S., Wong, T.-F., 2005. Experimental rock deformation – the brittle field. Springer (348 pp.).
Pedley, H.M., Grasso, M., 1992. Miocene syntectonic sedimentation along the western margins of the Hyblean-Malta platform: A guide to plate margin processes in the central Mediterranean. J. Geodyn. 15 (1–2), 19–37.
Russo, G., Giberti, G., Sartoris, G., 1997. Numerical modeling of surface deformation and mechanical stability of Vesuvius volcano, Italy. J. Geophys. Res. Solid Earth 102 (B11), 24785–24800.
Rust, D., Behncke, B., Neri, M., Ciocanel, A., 2005. Nested zones of instability in the Mount Etna volcanic edifice, Italy. J. Volcanol. Geotherm. Res. 144 (1–4), 137–153.
Sammis, C.G., Ashby, M.F., 1986. The failure of brittle porous solids under compressive stress states. Acta Metall. 34 (3), 511–526.
Scholz, C.H., 1968. Microfracturing and the inelastic deformation of rock in compression. J. Geophys. Res. 73 (4), 1417–1432.
Singh, B., 2011. Chapter 6 – rock mass rating. In: Goel, R.K., Singh, B. (Eds.), Engineering rock mass classification. Butterworth-Heinemann, Boston, pp. 45–62.
Stanchits, S., Vinciguerra, S., Dresen, G., 2006. Ultrasonic velocities, acoustic emission characteristics and crack damage of basalt and granite. In: Dresen, G., Zang, A., Stephansson, O. (Eds.), Rock damage and fluid transport, part I. Pageoph topical volumes, pp. 975–994 (Birkhäuser Basel).
Tibaldi, A., Lagmay, A.M.F., 2006. Interaction between volcanoes and their basement. J. Volcanol. Geotherm. Res. 158, 1–5. http://dx.doi.org/10.1016/j.jvolgeores.2006.04.011.
Torelli, L., Grasso, M., Mazzoldi, G., Peis, D., 1998. Plio–Quaternary tectonic evolution and structure of the Catania foredeep, the northern Hyblean Plateau and the Ionian shelf (SE Sicily). Tectonophysics 298 (1–3), 209–221.

van Wyk de Vries, B., Borgia, A., 1996. The role of basement in volcano deformation. Geol. Soc. Lond., Spec. Publ. 110 (1), 95–110.
van Wyk de Vries, B., Francis, P.W., 1997. Catastrophic collapse at stratovolcanoes induced by gradual volcano spreading. Nature 387 (6631), 387–390.
Vinciguerra, S., Trovato, C., Meredith, P.G., Benson, P.M., 2005. Relating seismic velocities, thermal cracking and permeability in Mt. Etna and Iceland basalts. Int. J. Rock Mech. Min. Sci. 42 (7–8), 900–910.
Xiao, X., Zhu, W., Evans, B., 2003. Deformation mechanisms and failure modes in Solnhofen limestone, *12th Panamerican conference on soil mechanics and geotechnical engineering, 1*, 39th U. S. Rock Mechanics Symposium.
Zhu, W., Baud, P., Wong, T.-f., 2010. Micromechanics of cataclastic pore collapse in limestone. J. Geophys. Res. Solid Earth 115 (B4), B04405.